

Titan's stratospheric C₂N₂, C₃H₄, and C₄H₂ abundances from Cassini/CIRS far-infrared spectra

N.A. Teanby^{a,*}, P.G.J. Irwin^a, R. de Kok^a, A. Jolly^b, B. Bézard^c, C.A. Nixon^d, S.B. Calcutt^a

^a Atmospheric, Oceanic & Planetary Physics, Department of Physics, University of Oxford, Clarendon Laboratory, Parks Road, Oxford, OX1 3PU, UK

^b LISA, Université Paris 12, 61 Av. Général de Gaulle, F-94010 Créteil Cedex, France

^c Observatoire de Paris, LESIA, Meudon, F-92195, France

^d Department of Astronomy, University of Maryland, College Park, MD 20742, USA

ARTICLE INFO

Article history:

Received 1 December 2008

Revised 13 March 2009

Accepted 18 March 2009

Available online 20 March 2009

Keywords:

Titan

Atmospheres, composition

ABSTRACT

Far-IR (25–50 μm, 200–400 cm⁻¹) nadir and limb spectra measured during Cassini's four year prime mission by the Composite InfraRed Spectrometer (CIRS) instrument have been used to determine the abundances of cyanogen (C₂N₂), methylacetylene (C₃H₄), and diacetylene (C₄H₂) in Titan's stratosphere as a function of latitude. All three gases are enriched at northern latitudes, consistent with north polar subsidence. C₄H₂ abundances agree with those derived previously from mid-IR data, but C₃H₄ abundances are about 2 times lower, suggesting a vertical gradient or incorrect band intensities in the C₃H₄ spectroscopic data. For the first time C₂N₂ was detected at southern and equatorial latitudes with an average volume mixing ratio of $5.5 \pm 1.4 \times 10^{-11}$ derived from limb data (>3-σ significance). This limb result is also corroborated by nadir data, which give a C₂N₂ volume mixing ratio of $6 \pm 3 \times 10^{-11}$ (2-σ significance) or alternatively a 3-σ upper limit of 17×10^{-11} . Comparing these figures with photochemical models suggests that galactic cosmic rays may be an important source of N₂ dissociation in Titan's stratosphere. Like other nitriles (HCN, HC₃N), C₂N₂ displays greater north polar relative enrichment than hydrocarbons with similar photochemical lifetimes, suggesting an additional loss mechanism for all three of Titan's main nitrile species. Previous studies have suggested that HCN requires an additional sink process such as incorporation into hazes. This study suggests that such a sink may also be required for Titan's other nitrile species.

© 2009 Elsevier Inc. All rights reserved.

1. Introduction

Titan's vast array of trace species are produced via an extensive photochemical cycle, which is discussed in detail in recent papers by Wilson and Atreya (2004) and Lavvas et al. (2008). This photochemistry is driven by dissociation of N₂, CH₄, and trace species into radicals and ions by solar UV and magnetospheric electrons in the upper atmosphere (>500 km). Galactic cosmic rays may also cause dissociation of nitrogen molecules in the lower atmosphere and provide an additional important source of nitrogen radicals (Capone et al., 1983). However, at present the exact mechanisms involved remain uncertain.

Observations of the abundance of trace gases can be compared to photochemical model predictions and be used to place constraints on reaction pathways. In addition, finite photochemical lifetimes of Titan's many trace species mean that they can be used as chemical tracers of Titan's atmospheric motion and seasonal

change (Teanby et al., 2009). Knowledge of trace species distribution throughout Titan's atmosphere is thus important for constraining atmospheric chemistry and dynamics. Here we determine the distributions of cyanogen (C₂N₂), methylacetylene (C₃H₄), and diacetylene (C₄H₂) from Cassini/CIRS far-IR nadir and limb spectra.

During the Voyager and Cassini epochs Titan's northern hemisphere was experiencing early spring and early-to-mid winter respectively. In northern winter the subsiding branch of a global meridional circulation cell supplies enriched air from the upper atmosphere photochemical production zone into the mesosphere and stratosphere, causing a build up of trace species around the north polar region where the subsidence occurs. The resulting increased abundances in Titan's northern hemisphere have allowed determinations of C₂N₂ at 50 and 70° N from Voyager (Kunde et al., 1981; Coustenis and Bézard, 1995) and a single determination from Cassini at 48° N (Teanby et al., 2006). C₂N₂ has not previously been observed at equatorial and southern latitudes during northern winter/spring due to its low abundance. At these latitudes analysis of Voyager/IRIS data gave 3-σ upper limits of $1-2 \times 10^{-9}$ (Coustenis and Bézard, 1995), whereas early analysis of Cassini/CIRS observations gave approximate 1-σ upper limits of

* Corresponding author. Fax: +44 1865 272923.

E-mail address: teanby@atm.ox.ac.uk (N.A. Teanby).

5×10^{-10} (Teanby et al., 2006). The distribution of C₂N₂ is thus at present very poorly constrained.

Previous studies of atmospheric composition have shown that there is an inverse relationship between photochemical lifetime and north polar relative enrichment (Teanby et al., 2008, 2009). However, nitrile compounds HCN and HC₃N display more enrichment than hydrocarbons with similar photochemical lifetimes. This suggested that there is an additional loss process for nitriles, which results in a steeper vertical profile and hence greater subsidence-induced enrichment in the north. With previously reported observations it is not possible to determine if C₂N₂ is also more enriched or if increased enrichment is peculiar to HCN and HC₃N.

C₃H₄ and C₄H₂ have strong emission features at both far- and mid-infrared wavelengths and their distributions have been previously determined in Titan's atmosphere with Voyager/IRIS (Kunde et al., 1981; Maguire et al., 1981; Coustenis and Bézard, 1995; Far- and Mid-IR) and Cassini/CIRS (Flasar et al., 2005; Coustenis et al., 2007; Teanby et al., 2008, 2009; Mid-IR only). Disc averaged abundances have also been determined for these gases from ISO data (Coustenis et al., 2003). For these gases analysis of Cassini/CIRS data has so far focused primarily on data from the mid-IR focal planes, which have superior spatial resolution and noise levels compared to the far-IR focal plane. Indeed, the distributions of C₃H₄ and C₄H₂ are most accurately mapped using the mid-IR CIRS focal planes and their global distributions for Titan's winter season are now relatively well constrained.

However, the far-IR does offer some advantages: (1) the main infrared emission feature of C₂N₂ lies in the far-IR and C₂N₂ features in the mid-IR are too weak to observe with CIRS; (2) the far-IR provides information at lower atmospheric levels than the mid-IR; (3) the far-IR emission lines are less affected by the hot stratopause in north polar regions, which leads to double peaked contribution functions for the mid-IR emission features of some species; and (4) the far-IR provides complementary information, which can aid interpretation of the mid-IR results. Comparing C₃H₄ and C₄H₂ abundances with previous higher spatial resolution mid-IR results also provides a check on our lower spatial resolution far-IR results.

Here, we use four years of far-IR Cassini/CIRS data taken over the prime mission to determine abundances of C₃H₄, C₄H₂, and C₂N₂ over Titan's globe. Measuring all three compounds simultaneously with the same focal plane means that C₃H₄ and C₄H₂ can be directly compared to C₂N₂. The photochemical lifetimes of these three gases (C₃H₄ = 0.8 yrs, C₄H₂ = 0.04 yrs, and C₂N₂ = 0.25 yrs defined at 300 km altitude from Wilson and Atreya, 2004) are such that C₃H₄ and C₄H₂ bracket the lifetime of C₂N₂, which should allow us to determine if it behaves like the other nitriles and also displays higher enrichment. This will provide us with insight into the photochemical processes that affect C₂N₂.

2. Observations

CIRS has three separate focal planes covering 10–600 cm⁻¹ (FP1), 600–1100 cm⁻¹ (FP3), and 1100–1500 cm⁻¹ (FP4). The mid-IR focal planes (FP3/4) comprise linear arrays of 10 pixels, with each pixel having a field-of-view approximately 0.27 × 0.27 mrad. The observations used here were taken with the far-IR focal plane (FP1), which consists of a single circular pixel with a Gaussian response of full-width half-maximum 2.5 mrad. The typical single-spectrum noise equivalent spectral radiance (NESR) at 0.5 cm⁻¹ spectral resolution are: 20 nW cm⁻² sr⁻¹/cm⁻¹ at 250 cm⁻¹ (FP1); 20 nW cm⁻² sr⁻¹/cm⁻¹ at 650 cm⁻¹ (FP3); and 4 nW cm⁻² sr⁻¹/cm⁻¹ at 1300 cm⁻¹ (FP4). The greater number of FP3/4 pixels allow larger averages to be formed, reducing noise levels to well below that in FP1. The CIRS instrument is described in detail by Kunde et al. (1996) and Flasar et al. (2004).

2.1. Nadir observations

Although the FP1 spectral range covers the peak in Titan's black body emission, the magnitude of emission features of individual gases above the background continuum are approximately the same as in the mid-IR. Therefore, many more FP1 observations are required to obtain comparable signal to noise. To maximise the signal-to-noise (S/N), observations were taken in a sit-and-stare mode, where the single FP1 pixel was centred on a single latitude and longitude for the duration of the observation. A spectral resolution of 0.5 cm⁻¹ was used so that discrete gas features could be resolved. To increase S/N of the emission features further, observations were typically off-nadir with emission angles of around 20–50°, which gave increased path length through the atmosphere and hence stronger emission features. Observations were typically obtained at distances of 200,000–300,000 km and had a duration of around 4 h, which allowed approximately 100–400 individual spectra to be measured each time.

Time constraints meant that only one or two of these observations could be taken per flyby, so full latitude coverage was built up gradually throughout the four year prime mission. The nadir observations used in this study are summarised in Tables 1–2 and Figs. 1–2.

The simple sit-and-stare viewing geometry allowed all spectra from a single observation to be averaged together to increase the S/N. This averaging typically reduced the NESR from 20 to 1 nW cm⁻² sr⁻¹/cm⁻¹ at 250 cm⁻¹. North of about 40° N polar enrichment of trace species meant that this was sufficient to measure abundances of all three gases. However, in the southern hemisphere and equatorial regions, gas abundances were much lower, especially for C₂N₂, which did not display a feature above the noise level in averaged spectra from single observations. Therefore, in an attempt to increase the S/N further, observations with similar latitude coverage and emission angle were averaged together into eight bins (A–H) as shown in Figs. 2 and 3. This type of binning was possible as latitude variations in temperature and composition are much smaller in the south than the north (Teanby et al., 2009).

The southern and equatorial regions should be representative of photochemical equilibrium and are important for constraining photochemical models. Previous studies have shown that abundances of most species start to increase northward of 30–40° N. The large FP1 FOV size (≈20° of latitude, see Tables 1 and 2) meant that to avoid the enriched region and obtain an abundance representative of the southern hemisphere the centre of the FOV should be south of 10–20° N. Therefore, an additional bin covering latitudes 90° S to 10° N and all emission angles was also used to obtain maximum possible S/N from the nadir observations for the southern hemisphere and equatorial regions.

2.2. Limb observations

Limb observations have the advantage of long atmospheric path lengths, so that emission features from trace gases are significantly enhanced compared to nadir and off-nadir measurements. For an atmospheric layer of thickness d and altitude z the increase in path length goes as $2\sqrt{2(R+z)/d+1}$, where R is Titan's radius. For our observations, which are typically sensitive to a 100 km thick layer of the stratosphere, this gives an approximate 14-fold increase in path length. Limb data thus provide the best means of measuring very low abundance trace species such as C₂N₂. However, high spectral resolution data taken close enough to Titan to resolve the limb are very limited, and are hence susceptible to the large single spectrum noise of FP1. Cassini must be closer than about 50,000 km for the limb projection of the 2.5 mrad FP1 pixel to resolve the stratosphere.

Table 1
Nadir observations used to determine gas VMRs north of 35° N. Northern enrichment of trace species provides sufficient S/N to determine gas abundances from individual observations. Rev = orbit number, N = number of spectra, SSLAT = sub spacecraft latitude, Long. = longitude, Lat. = latitude, latFOV = FOV latitude spread, e = emission angle, eFOV = range of emission angles across FOV.

Observation	Date	Rev	N	SSLAT (°N)	Long. (°W)	Lat. (°N)	latFOV (°)	e (°)	eFOV (°)
CIRS_005TL_FIRNADCMP003_PRIME	01/Apr/2005	005	240	-2.4	-150.3	45.3	25.4	52.2	28.4
CIRS_006TL_FIRNADCMP002_PRIME	16/Apr/2005	006	178	4.2	15.6	52.1	26.6	51.9	31.0
CIRS_025TL_FIRNADCMP003_PRIME	01/Jul/2006	025	185	-0.1	19.2	38.2	23.9	44.6	29.1
CIRS_035TL_FIRNADCMP003_PRIME	11/Dec/2006	035	305	31.0	129.0	61.9	23.2	33.4	24.3
CIRS_036TL_FIRNADCMP003_PRIME	27/Dec/2006	036	319	38.3	151.7	77.1	20.5	43.1	26.7
CIRS_039TL_FIRNADCMP002_PRIME	22/Feb/2007	039	23	51.2	-17.9	71.4	18.9	49.5	27.5
CIRS_040TL_FIRNADCMP002_PRIME	10/Mar/2007	040	106	44.9	-110.4	87.4	10.9	45.8	27.0
CIRS_040TL_GLOBMAP002_VIMS	10/Mar/2007	040	142	44.5	-83.4	72.8	23.7	36.8	33.2
CIRS_041TL_FIRNADCMP002_PRIME	26/Mar/2007	041	102	38.1	155.5	61.4	17.8	52.4	31.8
CIRS_042TL_FIRNADCMP002_PRIME	11/Apr/2007	042	272	30.7	-174.8	70.1	21.5	48.5	33.0
CIRS_043TL_FIRNADCMP002_PRIME	27/Apr/2007	043	104	23.2	-139.8	72.3	26.5	53.1	31.9
CIRS_045TL_FIRNADCMP002_PRIME	29/May/2007	045	346	9.9	-130.1	50.6	27.6	44.9	32.6
CIRS_048TL_FIRNADCMP002_PRIME	19/Jul/2007	048	260	-0.2	-14.5	47.3	31.6	51.5	36.6
CIRS_052TL_FIRNADCMP002_PRIME	19/Nov/2007	052	271	5.1	-172.9	39.0	25.0	47.9	33.5
CIRS_053TL_FIRNADCMP002_PRIME	05/Dec/2007	053	102	11.5	-143.8	57.3	25.7	49.5	29.3
CIRS_054TL_FIRNADCMP002_PRIME	21/Dec/2007	054	103	19.2	-93.4	59.3	20.7	56.4	36.9
CIRS_062TL_FIRNADCMP002_PRIME	25/Mar/2008	062	111	30.4	-56.1	59.6	17.5	54.5	32.3

Over the four years of the prime mission there have been six such limb observations at latitudes south of 10° N (Table 3). The distance of Cassini from Titan during these observations was 30,000–40,000 km and CIRS was used in a limb staring mode—with the observation time split equally between FOV central altitudes of 125 and 250 km. We selected the 125 km spectra as these had larger signal and sampled the stratosphere. These observations all had similar FOV sizes (116–156 km) and covered similar altitudes, so all the spectra were averaged together to form a single average limb spectrum, which is representative of the southern hemisphere stratosphere. As with the nadir observations, this type of averaging relies on the small temperature and compositional gradients that exist in the south.

3. Analysis

The far-IR emission features of our gases of interest occur at 220 cm⁻¹ (C₄H₂), 234 cm⁻¹ (C₂N₂), and 327 cm⁻¹ (C₃H₄), so we selected the spectral range 200–400 cm⁻¹ for our study. The continuum in this region is influenced by collision induced absorption (CIA) from N₂, CH₄, and H₂ pairs, Titan's photochemical hazes, and temperature.

3.1. Spectroscopic data

The spectroscopic data for the gases was the same as used by Teanby et al. (2008) except for C₂N₂ and C₄H₂. For C₂N₂ we used the linelist from GEISA2003 (Jacquinet-Husson et al., 2005) with some corrections and adjustments based on comparisons with spectroscopic measurements by Grecu et al. (1993). We first found an error in the intensities of the (02)² ← (01)¹, (03)¹ ← (02)², and (03)³ ← (02)² sub-bands and divided them by 2. We then rescaled all the intensities by a factor of 0.95, which was found to best reproduce the intensities observed by Grecu et al. (1993) in the fundamental band (01)¹ ← (00)⁰. For the N₂ broadening parameter at 296 K, we used the formula 0.12–0.00035|m| cm⁻¹ atm⁻¹, which reproduces well the measurements of Grecu et al. (1993) shown in their Fig. 5 (*m* is related to the total angular momentum quantum number *J* by *m* = *J* + 1 in the R-branch and *m* = –*J* in the P-branch). The exponent of temperature dependence was assumed to be 0.75 for all transitions. For C₄H₂ we used a recently updated linelist from Jolly et al. (2009).

CIA contributions from collision pairs N₂–N₂, CH₄–CH₄, H₂–H₂, N₂–CH₄, N₂–H₂, and CH₄–H₂ were calculated according to:

Borysow and Frommhold (1986a, 1986b, 1986c, 1987); Borysow (1991); Borysow and Tang (1993); and associated subroutines.

The spectral signatures of Titan's hazes were empirically derived from CIRS limb spectra by de Kok et al. (2007b). Our selected spectral range is affected by Titan's main haze (Haze 0) and a broad condensate feature centred at 220 cm⁻¹ (Haze B), which is present at high northern latitudes. The Haze 0/B notation follows that established by de Kok et al. (2007b).

3.2. Reference atmospheres

Our initial nominal Titan atmosphere had gas volume mixing ratios (VMRs) of: N₂ = 0.9859; CH₄ = 1.41 × 10⁻²; C₃H₄ = 1.2 × 10⁻⁸; C₄H₂ = 2 × 10⁻⁹; C₂N₂ = 2 × 10⁻¹⁰; H₂ = 1 × 10⁻³; and H₂O = 4 × 10⁻¹⁰. These values were based on previous measurements from CIRS (Flasar et al., 2005; Teanby et al., 2006), the Huygens GCMS (Niemann et al., 2005), and ISO (Coustenis et al., 2003).

Most gases condense in the lower stratosphere, where their abundance was set to the saturation vapour pressure. Tropospheric abundances were set to that at the tropopause cold trap, except for CH₄, where we used the Huygens GCMS profile. VMRs were assumed to be constant above the condensation level.

Stratospheric and mesospheric temperatures are now well determined for Titan's northern mid-winter season from previous analysis of CIRS limb and nadir data (Achterberg et al., 2008; Flasar et al., 2005; Teanby et al., 2007, 2008). We used a latitude dependent temperature profile interpolated from analysis of 0.5 and 2.5 cm⁻¹ data by Teanby et al. (2008) from orbit 36 (T22) on 26–27th December 2006, which had two complementary temperature mapping sequences covering both hemispheres. This constrained the temperature in the stratosphere where the gas emission lines are formed.

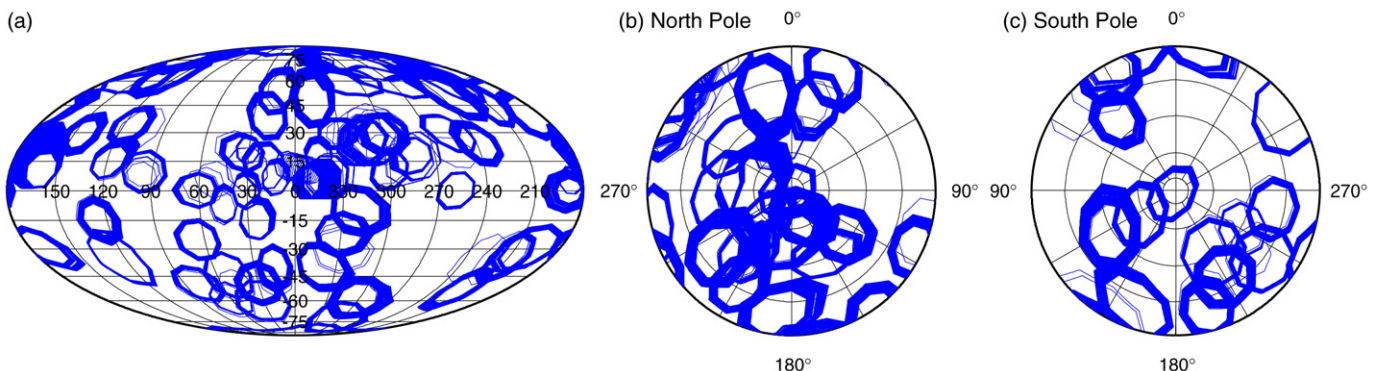
Note that for nadir spectra the continuum in the 200–400 cm⁻¹ region is sensitive to tropospheric temperature, which is difficult to determine and not easily separable from the effects of haze, CIA, and clouds. However, the emission lines of C₃H₄, C₄H₂, and C₂N₂ are all formed above this level in the stratosphere, for which the temperature is well defined. The excess emission from these gases is superimposed onto the continuum. Therefore, stratospheric abundances can be determined independently of tropospheric properties so long as the continuum is fitted by adjusting either tropospheric temperature or haze (Teanby et al., 2006).

Initial haze profiles were based on Cassini/CIRS and Huygens/DISR measurements. The main haze (haze 0 in de Kok et al.,

Table 2

Nadir observations taken south of 35° N, which have been binned to increase S/N. Bin indicates the bin each observation was included in.

Observation	Date	Rev	N	SSLAT (°N)	Long. (°W)	Lat. (°N)	latFOV (°)	e (°)	eFOV (°)	Bin
CIRS_024TI_FIRNADCMP003_PRIME	19/May/2006	024	350	0.0	125.8	-14.6	20.7	26.3	23.3	A, S
CIRS_040TI_FIRNADCMP001_PRIME	09/Mar/2007	040	159	-49.4	78.3	-49.8	20.1	27.5	22.5	A, S
CIRS_042TI_FIRNADCMP001_PRIME	10/Apr/2007	042	103	-36.1	30.8	-60.0	24.8	25.8	28.7	A, S
CIRS_043TI_FIRNADCMP001_PRIME	26/Apr/2007	043	263	-28.8	29.4	-49.2	23.2	22.6	24.0	A, S
CIRS_059TI_FIRNADCMP001_PRIME	22/Feb/2008	059	172	-22.5	62.6	-25.3	19.9	33.4	25.7	A, S
CIRS_062TI_CLOUDMAP001_VIMS	25/Mar/2008	062	208	-27.3	17.0	6.2	20.9	44.1	24.6	A, S
CIRS_067TI_FIRNADCMP001_PRIME	11/May/2008	067	48	-30.3	59.4	-58.3	20.7	31.6	22.1	A, S
CIRS_069TI_FIRNADCMP001_PRIME	27/May/2008	069	112	-27.7	51.6	-44.5	26.2	17.8	27.2	A, S
CIRS_00ATI_FIRNADCMP001_PRIME	26/Oct/2004	000	51	-14.6	-161.1	-29.5	23.5	42.9	33.6	B, S
CIRS_005TI_FIRNADCMP002_PRIME	31/Mar/2005	005	241	0.6	15.2	-39.2	23.8	42.2	25.9	B, S
CIRS_013TI_FIRNADCMP004_PRIME	22/Aug/2005	013	248	-9.2	-140.7	-51.6	23.0	45.1	25.1	B, S
CIRS_021TI_FIRNADCMP002_PRIME	27/Feb/2006	021	213	0.0	172.2	-28.9	21.3	48.8	31.3	B, S
CIRS_023TI_FIRNADCMP002_PRIME	01/May/2006	023	215	0.0	-150.3	-33.8	26.1	35.7	28.0	B, S
CIRS_030TI_FIRNADCMP002_PRIME	10/Oct/2006	030	340	-28.0	-57.2	-58.3	22.3	40.0	27.8	B, S
CIRS_035TI_FIRNADCMP023_PRIME	12/Dec/2006	035	156	-36.5	-53.7	-72.1	21.6	39.7	27.2	B, S
CIRS_036TI_FIRNADCMP002_PRIME	28/Dec/2006	036	136	-43.3	-42.0	-87.2	10.5	46.7	25.9	B, S
CIRS_045TI_FIRNADCMP001_PRIME	28/May/2007	045	231	-13.3	-28.7	-22.1	21.7	46.9	35.5	B, S
CIRS_048TI_FIRNADCMP001_PRIME	18/Jul/2007	048	96	0.0	125.4	-33.6	29.4	38.0	34.4	B, S
CIRS_053TI_FIRNADCMP001_PRIME	04/Dec/2007	053	223	-6.3	-18.1	-38.9	24.4	48.6	35.5	B, S
CIRS_025TI_FIRNADCMP008_ISS	02/Jul/2006	025	54	0.1	-172.8	5.1	13.5	19.9	15.9	C, S
CIRS_045TI_NIGHTWAC001_ISS	28/May/2007	045	78	-8.9	24.2	-4.5	3.9	5.4	4.5	C, S
CIRS_045TI_PHOTOMWAC001_ISS	28/May/2007	045	59	-13.1	12.4	6.3	17.2	21.9	19.0	C, S
CIRS_052TI_CLOUDMAP001_VIMS	18/Nov/2007	052	245	-2.9	-13.3	5.2	18.2	27.8	23.2	C, S
CIRS_059TI_PHOTOMWAC001_ISS	22/Feb/2008	059	56	-22.7	30.5	-0.3	18.4	23.7	19.5	C, S
CIRS_067TI_PHOTOMWAC001_ISS	12/May/2008	067	58	-30.3	44.7	-7.3	18.2	24.3	19.3	C, S
CIRS_019TI_FIRNADCMP002_PRIME	26/Dec/2005	019	124	0.0	54.9	0.2	16.9	49.9	28.8	D, S
CIRS_022TI_FIRNADCMP003_PRIME	18/Mar/2006	022	401	0.0	-171.8	-0.1	17.7	41.9	25.7	D, S
CIRS_029TI_FIRNADCMP003_PRIME	23/Sep/2006	029	312	13.1	96.7	10.1	18.7	41.6	27.1	D, S
CIRS_044TI_FIRNADCMP002_PRIME	13/May/2007	044	104	15.5	-101.8	0.6	17.7	44.8	26.6	D, S
CIRS_050TI_FIRNADCMP001_PRIME	01/Oct/2007	050	144	3.4	-37.4	-9.5	22.7	48.6	38.1	D, S
CIRS_00BTI_FIRNADCMP002_VIMS	13/Dec/2004	000	192	4.4	-10.1	17.3	15.3	16.2	16.6	E
CIRS_006TI_FIRNADCMP003_ISS	16/Apr/2005	006	26	4.5	30.9	20.5	14.0	19.3	15.5	E
CIRS_025TI_FIRNADCMP011_VIMS	01/Jul/2006	025	98	-0.1	19.4	12.1	23.2	24.4	26.9	E
CIRS_026TI_FIRNADCMP003_VIMS	21/Jul/2006	026	731	0.9	162.7	12.9	23.8	24.3	27.2	E
CIRS_00BTI_FIRNADCMP001_PRIME	12/Dec/2004	000	224	-9.2	118.6	15.4	19.1	46.3	27.0	F
CIRS_017TI_FIRNADCMP003_PRIME	28/Oct/2005	017	119	0.0	32.5	19.1	18.9	49.5	29.6	F
CIRS_022TI_FIRNADCMP008_PRIME	19/Mar/2006	022	83	0.0	-42.2	24.0	23.0	46.6	34.6	F
CIRS_025TI_FIRNADCMP002_PRIME	02/Jul/2006	025	307	0.1	-121.9	23.8	20.7	39.5	26.4	F
CIRS_059TI_FIRNADCMP002_PRIME	23/Feb/2008	059	98	26.3	-76.1	18.2	18.8	49.1	29.8	F
CIRS_062TI_GLOBMAP002_VIMS	26/Mar/2008	062	70	30.5	-80.7	18.7	24.5	34.9	31.5	F
CIRS_069TI_FIRNADCMP002_PRIME	28/May/2008	069	112	26.8	-60.7	10.6	18.2	45.0	26.3	F
CIRS_028TI_FIRNADCMP003_PRIME	07/Sep/2006	028	350	9.1	144.6	29.0	18.9	21.0	19.7	G
CIRS_030TI_FIRNADCMP003_PRIME	09/Oct/2006	030	286	21.6	115.4	33.7	19.2	22.0	22.1	G
CIRS_013TI_FIRNADCMP003_PRIME	21/Aug/2005	013	192	10.1	-27.5	29.2	14.8	51.6	27.7	H
CIRS_050TI_FIRNADCMP002_PRIME	02/Oct/2007	050	106	1.7	-107.4	29.1	18.7	51.8	31.0	H
CIRS_067TI_FIRNADCMP002_PRIME	12/May/2008	067	286	28.3	-62.5	29.8	20.0	42.5	29.6	H
CIRS_069TI_GLOBMAPFA002_VIMS	28/May/2008	069	68	26.7	-55.4	26.8	26.0	40.6	39.1	H

**Fig. 1.** Coverage of the nadir far-IR (FP1) observations used in this study. The four years of data give good coverage of all latitudes. Octagons show projected field-of-view sizes of each observation.

2007b) had a scale height of 65 km between 80 and 160 km altitude based on measurements by the Huygens Descent Imager Spectral Radiometer (DISR) instrument (Tomasko et al., 2008b).

This scale height is consistent with determinations from CIRS covering the same altitude range (de Kok et al., 2007b). For 160–240 km DISR measurements are not available and the profile of de Kok et al. (2007b) was used. Above 240 km constant haze particles/gram of atmosphere were assumed and below 80 km we assumed a constant number density. The 220 cm^{-1} broad condensate feature (haze B) had a profile that peaked at 140 km, as derived by de Kok et al. (2007b) at 70° N .

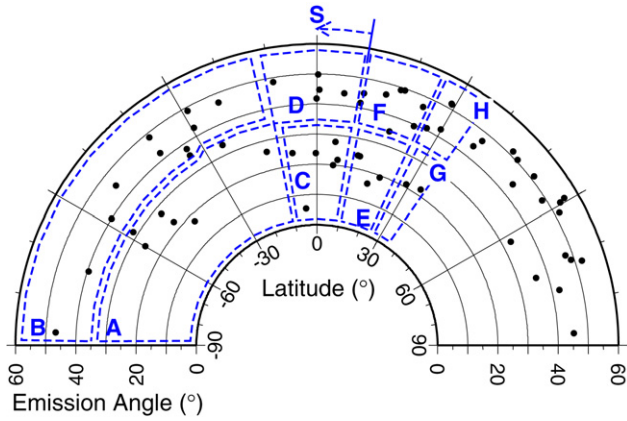


Fig. 2. Latitude and emission angle at the averaged field-of-view centre of each nadir observation. Dashed lines indicate the bins used to increase S/N at southern and equatorial latitudes.

3.3. Nadir composition inversion

To invert the observed spectra for composition we used the NEMESIS retrieval software (Irwin et al., 2008), which uses a constrained iterative non-linear inversion technique based on the correlated- k approximation (Lacis and Oinas, 1991). This keeps the composition as close as possible to the reference atmosphere, while fitting the data to within the measurement errors. The profiles of C_3H_4 , C_4H_2 , C_2N_2 , haze O, and haze B were scaled to provide the optimum fit to the averaged spectra in the $200\text{--}400\text{ cm}^{-1}$ range. In order to fit the continuum a slight adjustment to the temperature profiles was also required around the tropopause. However, we do not regard this as realistic because the temperature

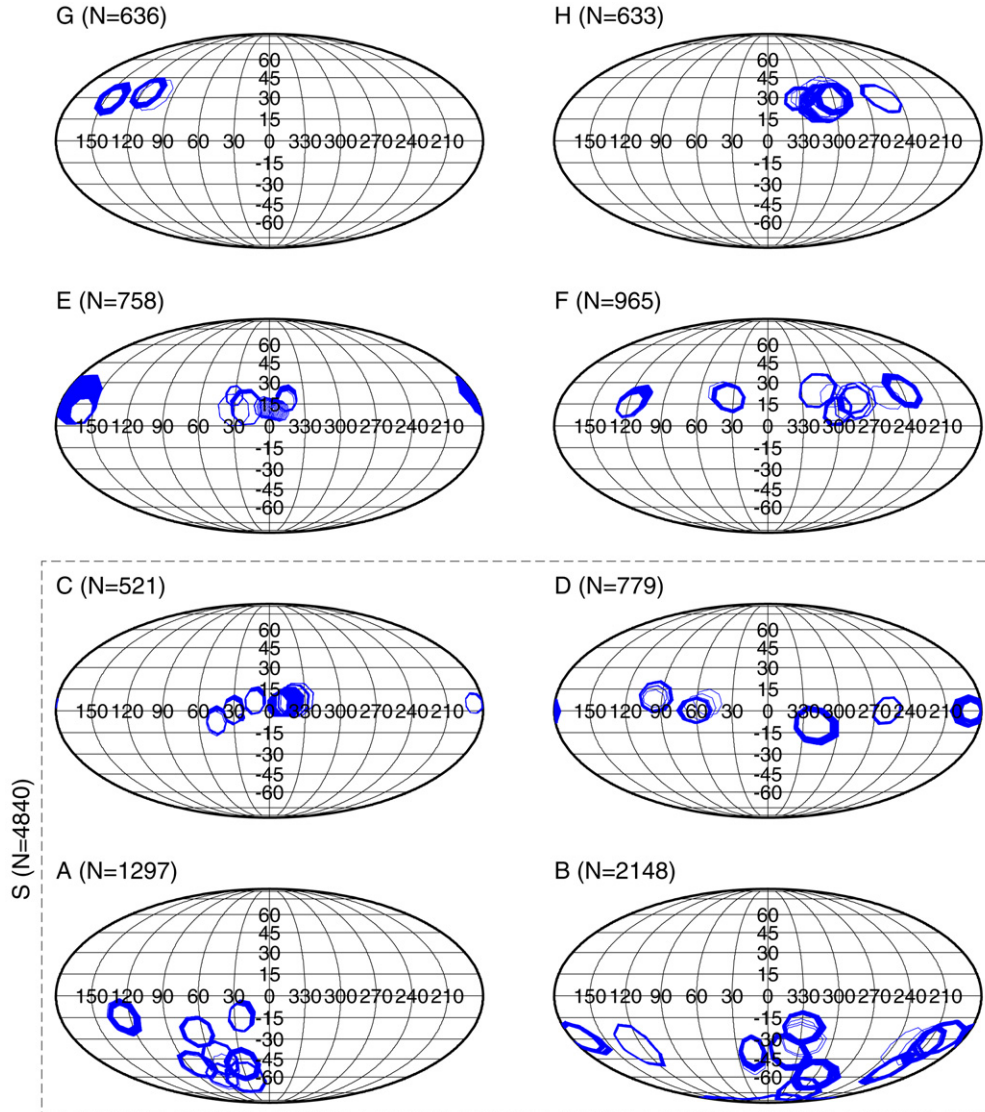


Fig. 3. Field-of-view projections of the nadir observations contained within each bin. N gives the number of spectra used from each bin after applying latitude and emission angle selection criteria. Bin S is not shown but includes all data south of 10° N .

Table 3

Limb observations used to produce the average southern hemisphere spectrum. Alt. = altitude of FOV centre and FOVsize = projected diameter of FOV on Titan's limb.

Observation	Date	Rev	N	SSLAT (°N)	Long. (°W)	Lat. (°N)	Alt. (km)	FOVsize (km)
CIRS_013TI_FIRLMBINT002_PRIME	22/Aug/2005	013	25	4.1	-47.3	-54.7	132.1	156.9
CIRS_013TI_FIRLMBINT003_PRIME	22/Aug/2005	013	23	-18.5	-46.8	-54.8	123.3	116.2
CIRS_028TI_FIRLMBINT002_PRIME	07/Sep/2006	028	25	11.1	65.4	-15.0	121.5	143.9
CIRS_052TI_FIRLMBINT001_PRIME	18/Nov/2007	052	23	-4.7	119.5	-80.1	128.5	152.1
CIRS_053TI_FIRLMBINT001_PRIME	04/Dec/2007	053	36	-11.2	114.4	0.0	121.6	155.1
CIRS_055TI_FIRLMBINT001_PRIME	05/Jan/2008	055	25	-21.8	134.2	-30.0	131.6	151.1

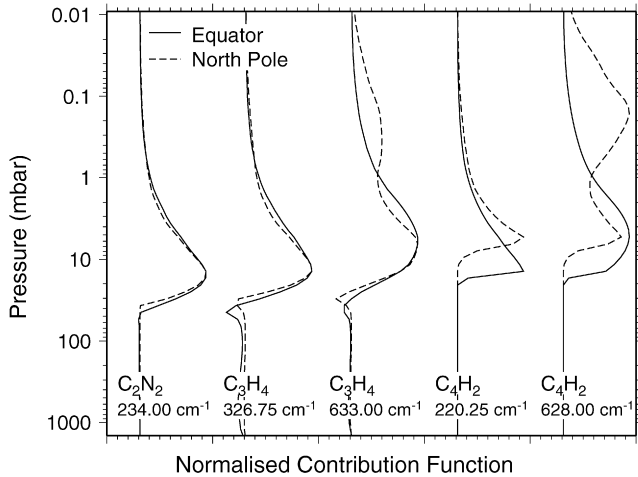


Fig. 4. Far- and mid-IR nadir contribution functions derived for reference atmospheres appropriate for equatorial (solid line) and north polar (dashed line) regions. Far-IR contribution functions (234, 326.75, and 220.25 cm⁻¹) typically sound lower atmospheric levels than those for the mid-IR (633, 628 cm⁻¹). Northern mid-IR contribution functions exhibit double peaks caused by the hot northern stratopause. Condensation of C₄H₂ causes far- and mid-IR observations to probe similar pressure levels at the equator.

there is well constrained by the Huygens probe. The difference may be due to extra haze opacity or inaccuracies in the CIA coefficients at the very low temperature of Titan's tropopause (70 K), as suggested by Tomasko et al. (2008a).

Fig. 4 shows the contribution functions (rate of change of radiance with abundance) for C₃H₄, C₄H₂, and C₂N₂ for the mid- and far-IR emission peaks for nominal equatorial and north polar atmospheres. The north polar atmosphere had a temperature appropriate for around 80° N and had gas abundances increased to 3 × 10⁻⁹ (C₂N₂), 4 × 10⁻⁸ (C₃H₄), and 4 × 10⁻⁸ (C₄H₂). This figure shows that the far-IR contribution functions for C₂N₂ and C₃H₄ tend to probe a consistent pressure level that is not strongly dependent on latitude, whereas the mid-IR contribution functions tend to develop a second peak for northern latitudes at around 0.1 mbar due to the hot north polar stratopause (Achterberg et al., 2008; Teanby et al., 2008).

In general, the far-IR data also probe lower in the atmosphere. However, the low saturation vapour pressure of C₄H₂ causes condensation to occur at lower pressures than for C₃H₄ and C₂N₂. This effectively “crops” the C₄H₂ contribution functions and as a result both mid- and far-IR spectra probe similar pressure levels at the equator. The far-IR contribution function peak of C₄H₂ is shifted to higher altitudes towards the north pole due to enhanced condensation in the cold winter stratosphere.

3.4. Limb composition inversion

To retrieve abundances from the averaged limb spectra we again used the NEMESIS retrieval software (Irwin et al., 2008), which has been previously used for Titan limb data analysis by de Kok et al. (2007a) and Teanby et al. (2007). However, for our study

we effectively have one measurement at one altitude with a very large field of view covering the entire stratosphere. This makes the inversion problem very non-unique so certain simplifications were required. First, as C₂N₂ was the main target of this dataset, we fitted a reduced spectral range covering 219.5–237 cm⁻¹. Second, the temperature profile was fixed to that in the latitude-dependent reference atmosphere. Third, C₄H₂, C₂N₂, and haze 0 were scaled to obtain the best fit. The large FOV size was taken into account by using the method of Teanby and Irwin (2007) with 7 FOV averaging points, which reduced systematic effects to below the level of the measurement errors.

3.5. Upper limits

Because of the low abundance of C₂N₂ at equatorial and southern latitudes, it may be more appropriate to consider upper limits instead of absolute abundance determinations.

To calculate upper limits we require the error weighted misfit χ^2 between the measured spectrum $r_{\text{meas}}(\nu_i)$ and the fitted spectrum $r_{\text{fit}}(\nu_i, x_j)$, defined by:

$$\chi_j^2 = \sum_{i=1}^M \frac{(r_{\text{meas}}(\nu_i) - r_{\text{fit}}(\nu_i, x_j))^2}{\sigma_i^2}, \quad (1)$$

where the spectrum is measured at $i = 1, \dots, M$ wavenumbers ν_i , σ_i is the noise on the i th wavenumber, and x_j is the volume mixing ratio of the gas we are determining the upper limit for. We refer to χ_0 as the misfit when the VMR of the gas is set to zero ($x_0 = 0$).

To calculate upper limits we used the method from the previous sections to fit the continuum. The gas of interest was then set to zero abundance, which gave χ_0^2 . The abundance x_j of each gas was then gradually increased and used to calculate the misfit χ_j^2 and change in the misfit $\Delta\chi_j^2 = \chi_j^2 - \chi_0^2$ for each test VMR. The minimum $\Delta\chi^2$, $\Delta\chi_{\text{min}}^2$, corresponded to the best fitting VMR. Because the gas emission features are distinct, each gas can be considered separately, giving 1 degree of freedom in each case. Therefore, a 1-, 2-, or 3- σ detection is made if the change in the misfit $\Delta\chi_{\text{min}}^2$ is less than -1, -4, or -9 respectively (Press et al., 1992). If no detection is made, then 1-, 2-, or 3- σ upper limits are given by the VMR for which $\Delta\chi^2 = +1, +4, \text{ or } +9$. 1- σ errorbars were defined by the VMRs for which $\Delta\chi^2 = \Delta\chi_{\text{min}}^2 + 1$.

4. Results

Fig. 5 shows example fits to the measured nadir spectra for a range of latitudes. It can be seen from the raw data that the emission features from C₃H₄, C₄H₂, C₂N₂, and haze B increase towards the north pole—suggesting increased abundances.

Fig. 6 shows a close up of the C₄H₂ and C₂N₂ spectral region for the binned observations. At southern and equatorial latitudes a visual inspection of the fits and measurement errors suggests that the abundances derived for C₂N₂ may not be reliable. This was investigated further by determining formal upper limits as outlined in Section 3.5. Fig. 7 shows the variation of $\Delta\chi^2$ as a function of

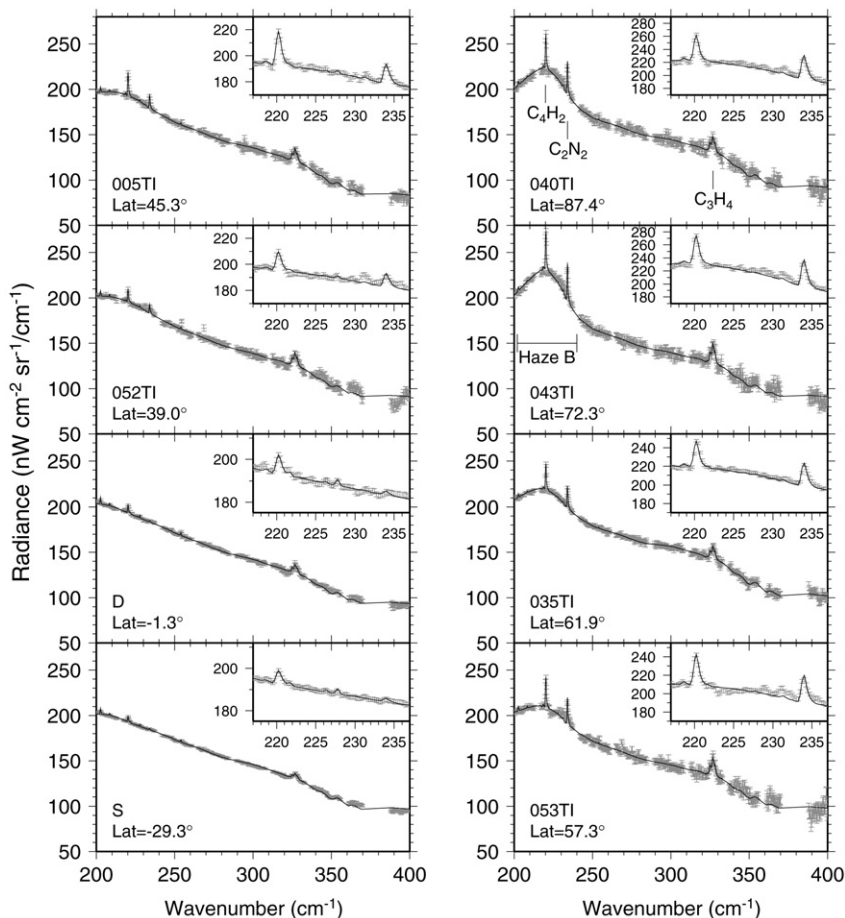


Fig. 5. Example fits (solid lines) to the measured nadir spectra (grey with errors) at representative latitudes. Inserts show a close up of the C_4H_2 and C_2N_2 features. The strengths of the C_2N_2 , C_3H_4 , and C_4H_2 emission features increase toward the north—indicating increased abundances. Gaps in the data correspond to electrical noise spikes, which have been removed from the spectra before processing.

VMR for C_2N_2 derived using the multi-observation averages (BIN A–H, and BIN S). The $\Delta\chi^2$ variation for C_4H_2 , which is reliably determined at southern latitudes, is also shown for comparison.

For C_4H_2 all bins display a deep minima with a $\Delta\chi_{\min}^2$ of at least -30 (corresponding to a detection with over $5\text{-}\sigma$ significance). This is consistent with the obvious spectral signature of C_4H_2 in southern and equatorial spectra visible in Fig. 6.

However, the C_2N_2 emission peak is a much weaker feature. Bin A shows no evidence for C_2N_2 and increasing the VMR degrades the fit (increases $\Delta\chi^2$), suggesting a $3\text{-}\sigma$ upper limit of 12×10^{-11} . However, for bins B, C, D there is evidence for C_2N_2 at the $2\text{-}\sigma$ level ($\Delta\chi_{\min}^2 \leq -4$), suggesting VMRs of $8\text{--}10 \times 10^{-11}$. Bin S—containing an average of all southern and equatorial spectra up to 10° N—gives a C_2N_2 $2\text{-}\sigma$ detection of $6 \pm 3 \times 10^{-11}$, or alternatively a $3\text{-}\sigma$ upper limit of $<17 \times 10^{-11}$.

Bins E, F, G, and H, which sample the northern most latitudes give detections above the $3\text{-}\sigma$ level ($\Delta\chi_{\min}^2 \leq -9$). At these northern latitudes the polar enrichment is starting to become visible due in-part to the large FOV size.

Fig. 8 shows the fit to the averaged limb spectrum and the $\Delta\chi^2$ variation for C_2N_2 . Despite the fact that this average only contains 157 spectra, the increased path length from limb geometry allows C_2N_2 to be detected above the $3\text{-}\sigma$ level, with a VMR of $5.5 \pm 1.4 \times 10^{-11}$. This is the first detection of C_2N_2 at equatorial and southern latitudes and is consistent with the nadir result from Bin S of $6 \pm 3 \times 10^{-11}$.

The VMRs and upper limits of each gas derived from nadir and limb data are given in Table 4. Fig. 9 shows the dependence of

VMR on latitude for each gas. Limb and nadir VMRs are consistent to within the errors.

5. Discussion

Fig. 9 shows that all three gases increase in abundance towards the north pole. Previous work (Flasar et al., 2005; Teanby et al., 2006, 2008, 2009; Coustenis et al., 2007) show that this is true for most short (less than a Titan year) lifetime gases and can be explained by subsidence of enriched air from the high altitude production zone into the winter stratosphere.

5.1. Comparison of C_3H_4 and C_4H_2 abundances with CIRS mid-IR results

Fig. 9 also shows the mid-IR results for orbit 36 (T22) from Teanby et al. (2009) for comparison. The plotted mid-IR abundances have been re-calculated using the new C_4H_2 linelist (Jolly et al., 2009) so a fair comparison can be made (N.B. although the new linedata improved the mid-IR fits, the differences in derived abundances were within the quoted uncertainties).

For C_4H_2 the mid- and far-IR results agree very well for latitudes south of 45° N. This is because the low saturation vapour pressure of C_4H_2 causes condensation, which crops the contribution functions of the mid- and far-IR emission features at similar levels (Fig. 4). Therefore, both wavelength ranges give consistent results. Note that this agreement also shows that the band strength ratio between mid- and far-IR linelists in the new Jolly et al. (2009) linedata is consistent. At latitudes north of 45° N the far-IR data used here gives lower abundances. This is due to the hot

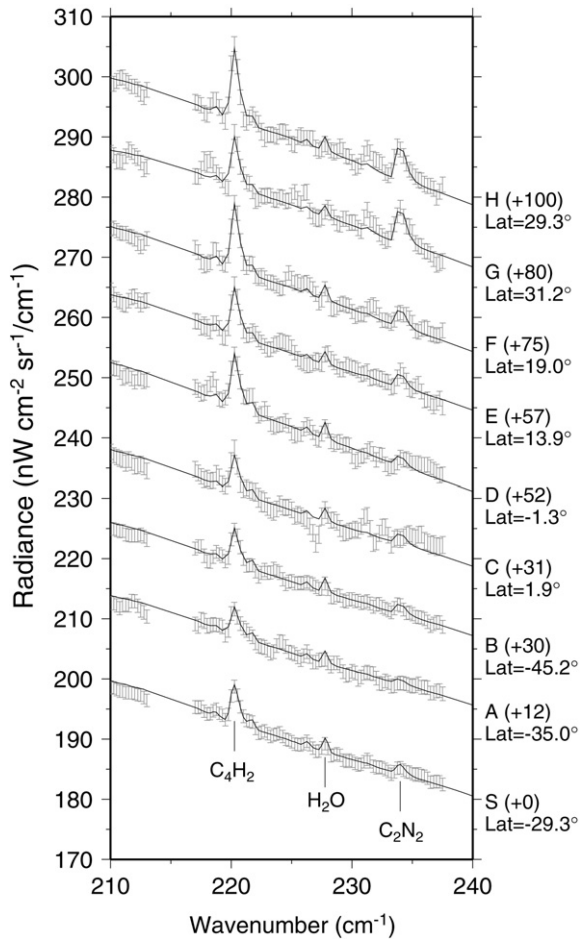


Fig. 6. Zoom-in of fits to the binned nadir spectra around the C_2N_2 and C_4H_2 emission features. C_2N_2 emission is obvious for northern bins (E–H), but is much weaker in the south (A–D, S). C_4H_2 is visible at all latitudes. Spectra are offset for clarity by the amount given in brackets.

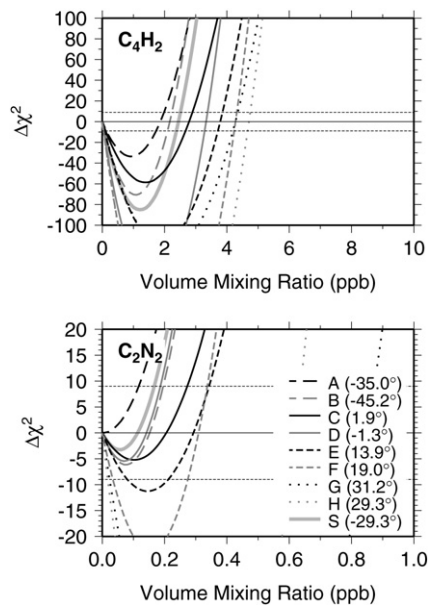


Fig. 7. Change in the misfit $\Delta\chi^2$ between modelled and measured binned nadir spectra caused by increasing the VMRs of C_2N_2 and C_4H_2 . Horizontal dashed lines indicate the levels of $3\text{-}\sigma$ detection (lower line) and upper limits (upper line). C_4H_2 has deep minima for all bins and is detected well above the $3\text{-}\sigma$ level. C_2N_2 has a $3\text{-}\sigma$ detection ($\Delta\chi^2 < -9$) for bins E–H, but is only detected at or below the $2\text{-}\sigma$ level ($\Delta\chi^2 < -4$) for southern bins.

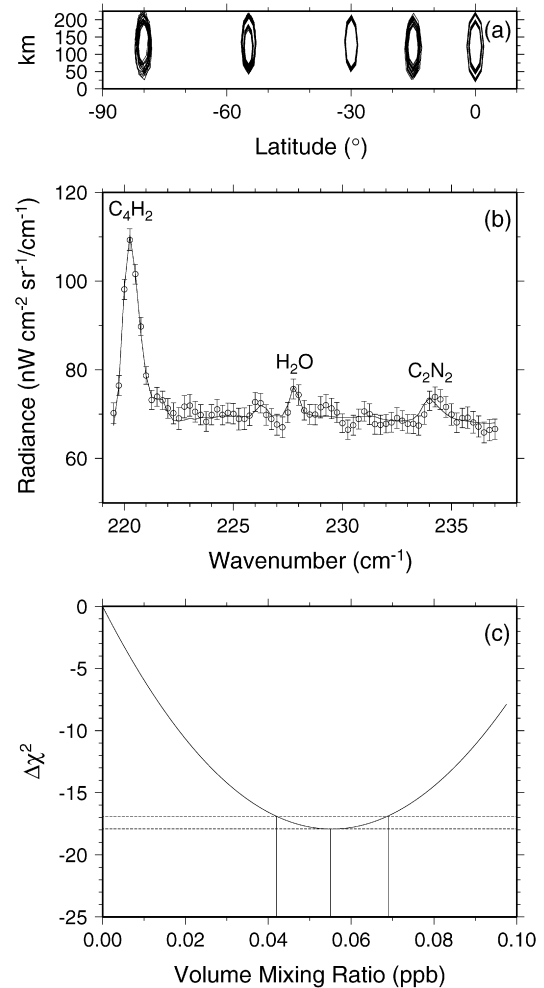


Fig. 8. Southern hemisphere and equatorial averaged limb data. (a) Projected field-of-views of the individual spectra used to form the average limb spectrum. Note that FOVs should be circular but have been distorted by the vertical exaggeration of the plot. (b) Fit (solid line) to the measured average spectrum (circles with error bars). N.B. the H_2O abundance was reduced from 4×10^{-10} to $1.8 \pm 0.5 \times 10^{-10}$ to give the best fit to the data. (c) $\Delta\chi^2$ as a function of C_2N_2 volume mixing ratio. Horizontal lines show $\Delta\chi_{\min}^2$ and $\Delta\chi_{\min}^2 + 1$, which were used to determine the best fit and $1\text{-}\sigma$ errors. The best fit is obtained with a VMR of $5.5 \pm 1.4 \times 10^{-11}$.

stratopause in the north, which causes a double peaked contribution function in the mid-IR and results in sounding higher in the atmosphere. A positive vertical gradient in the VMR profile would then result in a lower abundance from the far-IR spectra, in keeping with what we see here. The difference between VMRs derived from mid- and far-IR data, which should probe approximately 0.2 and 6 mbar for the mid-IR (double peaked contribution function) and 6 mbar for the far-IR, is only about a factor of two. This is much less than the equatorial gradient between the 0.2 and 6 mbar pressure levels of ≈ 10 (Vinatier et al., 2007) and suggests that the profile of C_4H_2 has shallowed significantly at northern latitudes. This shallowing would be expected due to increased vertical mixing caused by downward advection of enriched air from the mesosphere and has been previously noted for HCN by Vinatier et al. (2007).

For C_3H_4 , the mid- and far-IR results have similar trends, but are offset from each other. In fact scaling the far-IR results by 2 almost exactly matches the mid-IR results (Fig. 9). This discrepancy could be due to a vertical gradient in C_3H_4 combined with sounding different atmospheric levels in the far- and mid-IR: the far-IR contribution function peaks at 15 mbar while the mid-IR contribution function peaks at 6 mbar. However, another

Table 4
Volume mixing ratios determined for C_2N_2 , C_4H_2 , and C_3H_4 from binned nadir observations (top), individual nadir observations (middle), and averaged southern hemisphere limb spectrum (bottom). VMR = volume mixing ratio in ppb; VMRerr = 1- σ errors in ppb; Σ = significance of detection if less than 3- σ ; and 3- σ_{up} = upper limit (3- σ) for detections with $\Sigma < 3$ in ppb.

Observation	Lat. (°N)	C_2N_2			C_4H_2		C_3H_4		
		VMR	VMRerr	Σ	3- σ_{up}	VMR	VMRerr	VMR	VMRerr
BIN_A	-35.0	0.00	0.04	-	0.12	1.09	0.19	1.20	0.25
BIN_B	-45.2	0.08	0.03	2.48	0.20	1.18	0.15	2.43	0.18
BIN_C	1.9	0.10	0.05	2.28	0.27	1.42	0.21	3.15	0.30
BIN_D	-1.3	0.07	0.03	2.33	0.19	1.65	0.16	3.50	0.20
BIN_E	13.9	0.15	0.05	>3	-	1.90	0.21	4.43	0.28
BIN_F	19.0	0.15	0.04	>3	-	2.11	0.17	4.62	0.23
BIN_G	31.2	0.42	0.05	>3	-	2.12	0.23	5.48	0.34
BIN_H	29.3	0.31	0.04	>3	-	2.32	0.18	5.01	0.25
BIN_S	-29.3	0.06	0.03	1.80	0.17	1.35	0.15	2.60	0.17
CIRS_025TL_FIRNADCMP003_PRIME	38.2	0.65	0.06	>3	-	3.91	0.26	7.27	0.45
CIRS_052TL_FIRNADCMP002_PRIME	39.0	0.52	0.05	>3	-	2.88	0.22	6.71	0.35
CIRS_005TL_FIRNADCMP003_PRIME	45.3	0.75	0.05	>3	-	5.31	0.25	6.56	0.38
CIRS_048TL_FIRNADCMP002_PRIME	47.3	0.92	0.06	>3	-	4.88	0.24	8.38	0.42
CIRS_045TL_FIRNADCMP002_PRIME	50.6	1.01	0.06	>3	-	5.81	0.27	8.47	0.46
CIRS_006TL_FIRNADCMP002_PRIME	52.1	0.88	0.06	>3	-	5.50	0.28	7.32	0.48
CIRS_053TL_FIRNADCMP002_PRIME	57.3	1.83	0.10	>3	-	8.09	0.39	11.95	0.74
CIRS_054TL_FIRNADCMP002_PRIME	59.3	1.78	0.10	>3	-	8.49	0.38	14.12	0.73
CIRS_062TL_FIRNADCMP002_PRIME	59.6	2.03	0.09	>3	-	9.22	0.37	12.37	0.69
CIRS_041TL_FIRNADCMP002_PRIME	61.4	1.79	0.10	>3	-	9.19	0.41	12.26	0.78
CIRS_035TL_FIRNADCMP003_PRIME	61.9	2.09	0.10	>3	-	8.56	0.37	12.67	0.80
CIRS_042TL_FIRNADCMP002_PRIME	70.1	2.12	0.10	>3	-	11.38	0.38	14.02	0.73
CIRS_039TL_FIRNADCMP002_PRIME	71.4	2.68	0.21	>3	-	14.85	0.95	13.70	1.70
CIRS_043TL_FIRNADCMP002_PRIME	72.3	2.76	0.12	>3	-	10.93	0.45	14.48	0.88
CIRS_040TL_GLOBMAP002_VIMS	72.8	2.59	0.14	>3	-	11.94	0.50	15.95	1.13
CIRS_036TL_FIRNADCMP003_PRIME	77.1	2.99	0.11	>3	-	12.25	0.39	15.01	0.79
CIRS_040TL_FIRNADCMP002_PRIME	87.4	2.84	0.14	>3	-	10.83	0.50	13.32	1.01
SOUTHERN LIMB AVERAGE	-35.7	0.055	0.014	>3	-	1.44	0.06	-	-

possible contribution to the discrepancy is the accuracy of the relative band strengths in the C_3H_4 linedata. Our linedata has a mid-IR (ν_9) to far-IR (ν_{10}) band ratio of 4.28 based on studies by Horneman et al. (1989) and Horneman (1989) (ν_{10}) and Blanquet et al. (1992) (ν_9). However, earlier band strengths measurements by Bode et al. (1980) and Kondo and Koga (1978) suggest band ratios of $\nu_9/\nu_{10} = 5.67$ and $\nu_9/\nu_{10} = 5.26$, respectively. Taking into account a possible 30% error in the band ratio implies a VMR ratio from 6 to 15 mbar of 2 ± 0.6 . This is consistent with an extrapolation of the C_3H_4 profile at 15° S derived by Vinatier et al. (2007), which gives a value of around 1.5.

5.2. Nitrile enrichment

Under equilibrium photochemical conditions and in the absence of bulk vertical advection, chemical species produced in the upper atmosphere by photochemistry are transported to the lower mesosphere and stratosphere by vertical mixing processes. This takes time, so species with shorter photochemical lifetimes will have decayed more by the time they reach lower atmospheric levels, leading to steeper vertical gradients than longer lifetime species. Therefore, in general the vertical gradient of each species would be expected to be inversely proportional to its photochemical lifetime. In regions of downward advection, such as the northern winter pole, the steeper vertical gradients of short lifetime species would then lead to greater relative enrichment. This simplified scenario provides a simple way of comparing predictions from photochemical models to observed latitude distributions, with any differences indicating that additional processes may be at work.

Previous nadir studies of Titan's trace species (Teanby et al., 2008, 2009) have shown that there does indeed appear to be an inverse relationship between photochemical lifetime and the relative enrichment in the north polar region compared to equatorial regions. These studies also show that HCN and HC_3N have much greater north polar enrichment than hydrocarbons with sim-

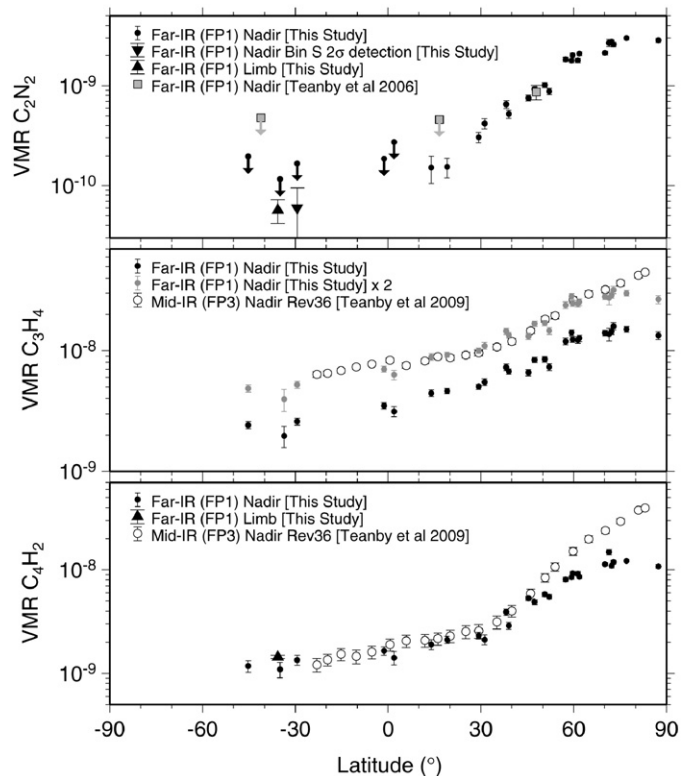


Fig. 9. VMRs of each gas as a function of latitude. Downward arrows for C_2N_2 indicate 3- σ upper limits from this study and approximate 1- σ upper limits from Teanby et al. (2006). Mid-IR results from Teanby et al. (2009) are also shown (recalculated using new C_4H_2 linedata). A scaling of 2 is required to match the C_3H_4 far- and mid-IR results. C_4H_2 results are consistent at equatorial latitudes but diverge north of 45° N due to changing mid-IR contribution functions.

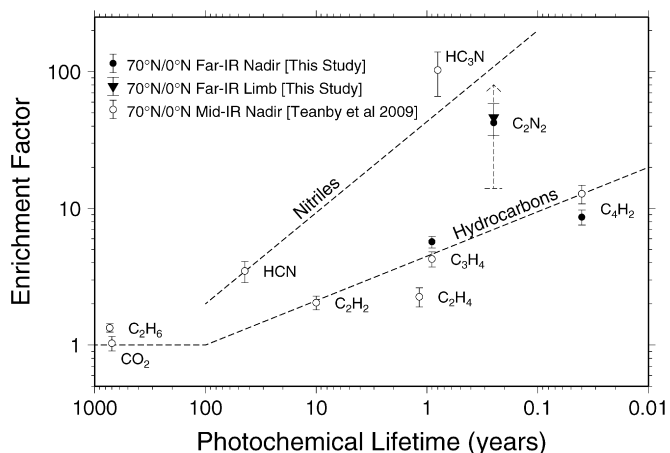


Fig. 10. Enrichment ratio versus photochemical lifetime (in Earth years). Mid-IR results from (Teanby et al., 2009) are shown for context. C_2N_2 behaves similarly to other nitriles (HCN, HC_3N) and exhibits more enrichment than hydrocarbons. The dashed arrow is based on a C_2N_2 upper limit of 17×10^{-11} derived from Bin S. Error bars give the $1\text{-}\sigma$ uncertainty on the enrichment ratios determined by combining the errors at 0° N and 70° N. Dashed lines give best fitting trend lines for nitriles and hydrocarbons.

ilar photochemical lifetimes—suggesting steeper vertical gradients than expected and that the overall lifetimes of HCN and HC_3N are less than expected from photochemistry alone. This is supported by analysis of limb data by Vinatier et al. (2007), who found that the vertical gradient of HCN around the equator was much steeper than could be explained by present photochemical models. They concluded that incorporation of HCN into photochemical haze was a likely possibility.

Fig. 10 shows the ratio of VMR at 70° N/ 0° N as a function of photochemical lifetime at 300 km from Wilson and Atreya (2004). Values at 70° N were taken from a smooth spline fit to the latitude-VMR datapoints in Fig. 9. Values for 0° N were taken from Bin S for the nadir points and additionally from the southern hemisphere limb average for C_2N_2 . An upper limit of 17×10^{-11} was used to draw the C_2N_2 bounding arrow for the nadir case. The mid-IR results from Teanby et al. (2009) are also shown for context. Both nadir and limb data show that C_2N_2 is more enriched in the north relative to the equator than would be expected from its photochemical lifetime alone—just like the other nitriles HCN and HC_3N . This suggests that all three of Titan's main nitrile species have shorter overall lifetimes than expected and additional loss processes are required in the lower atmosphere to steepen their vertical gradients.

Following laboratory experiments to create tholin compounds, McKay (1996) suggested that haze formation could be a significant sink for nitrogen. This initial idea was extended by Lara et al. (1999), who introduced a sink term for HCN in order to bring photochemical model results and observed gas profiles into agreement. Recently Vinatier et al. (2007) have derived a HCN sink term of similar magnitude. Photopolymerisation of nitrile compounds in the lower atmosphere and subsequent incorporation into haze particles could provide one such sink mechanism for nitrile compounds (Clarke and Ferris, 1996). Our study suggests that HCN, HC_3N , and C_2N_2 all require additional sink terms and that whatever processes are occurring act on multiple nitrile species and are not limited to HCN.

5.3. Implications of C_2N_2 equatorial abundance

Our detection of C_2N_2 at southern and equatorial latitudes can be compared to predictions from photochemical models. In Titan's upper atmosphere N atoms formed by photolysis and electron

impact are involved in many competing photochemical processes, most of which lead to the production of HCN (Wilson and Atreya, 2004). For example the main HCN forming pathway is $N + CH_3 \rightarrow H_2CN + H \rightarrow HCN + H_2$. Photolysis of HCN then produces CN radicals, which are used to form more complex nitriles such as HC_3N (via $CN + C_2H_2$). C_2N_2 is thought to be formed by N-atom addition to C_2H_2 , but the net effect of competition for N atoms is that relatively small amounts of C_2N_2 are formed in the upper atmosphere.

Capone et al. (1983) show that galactic cosmic rays could cause dissociation of N_2 molecules in the stratosphere. This additional source of N atoms could increase production of C_2N_2 by N-atom addition to C_2H_2 , which is abundant in the stratosphere, whereas the CH_3 and CN radicals that form HCN and HC_3N are not. Therefore, from Titan's three main nitrile species (HCN, HC_3N , C_2N_2) we would expect C_2N_2 to be most effected by cosmic rays. C_2N_2 abundance should thus provide the most sensitive chemical indicator of cosmic ray activity.

The photochemical model of Wilson and Atreya (2004) predicts a C_2N_2 abundances of around 10^{-9} if cosmic rays are active in the stratosphere and $<10^{-14}$ if not (at the 100 km/10 mbar level). However, the effects of cosmic rays are not well constrained and a recent model by Lavvas et al. (2008) predicts 5×10^{-13} with cosmic rays and $<10^{-14}$ without. The abundances with cosmic rays active in the two models are very different, illustrating uncertainties in the mechanism, but in both cases our detections of $5.5 \pm 1.4 \times 10^{-11}$ (limb) and $6 \pm 3 \times 10^{-11}$ (nadir, $2\text{-}\sigma$) are closest to abundances predicted by including cosmic ray effects.

6. Conclusions

Four years of far-IR data from Cassini/CIRS have been used to provide the most complete measurements of C_2N_2 in Titan's atmosphere to date. The C_2N_2 VMR has a maximum value of 3.5×10^{-9} in Titan's northern hemisphere. At southern and equatorial latitudes we find average VMRs of $5.5 \pm 1.4 \times 10^{-11}$ from limb data and $6 \pm 3 \times 10^{-11}$ from nadir data. The nadir detection is only significant at the $2\text{-}\sigma$ level and a more robust interpretation is a $3\text{-}\sigma$ upper limit of $<17 \times 10^{-11}$. Comparing the measured southern and equatorial C_2N_2 abundance with photochemical models (Wilson and Atreya, 2004; Lavvas et al., 2008) suggests that galactic cosmic rays may be an important source of C_2N_2 in the stratosphere.

C_3H_4 and C_4H_2 VMRs were also determined. C_3H_4 is consistently 2 times higher when measured in the mid-IR than when measured in the far-IR. This could be due to a vertical gradient between contribution function peaks at 15 mbar (far-IR) and 6 mbar (mid-IR), although possible discrepancies in the relative band strengths of mid- and far-IR C_3H_4 linedata may also contribute.

C_4H_2 mid- and far-IR VMR determinations are consistent south of 45° N, but differ by up to a factor of 2 near the north pole. This is most likely due to the hot polar stratopause, which causes mid- and far-IR contribution functions to sound different levels. However, a factor of 2 difference is not large and suggests a much shallower vertical gradient in polar regions than that derived previously at equatorial latitudes—in keeping with subsidence-driven enrichment in the north. The consistency of the results at equatorial and southern latitudes provides additional validation for the recent C_4H_2 linelist by Jolly et al. (2009).

A plot of photochemical lifetime versus relative north polar enrichment shows that all the major nitrile species in Titan's atmosphere (HCN, HC_3N , and C_2N_2) display relatively more enrichment than hydrocarbons with similar photochemical lifetimes. If enrichment is caused solely by subsidence coupled with a vertical gradient this suggests that nitriles have a steeper initial vertical gradient, perhaps caused by additional loss processes in the

lower atmosphere leading to shorter overall lifetimes. Incorporation into Titan's photochemical hazes could provide a sink for the nitriles as suggested by McKay (1996), Lara et al. (1999), Vinatier et al. (2007), and Teanby et al. (2009). However, this interpretation could be too simplistic and other complicating factors such as species-dependent production altitudes, influence of thermospheric dynamics, or complex polar chemistry could also affect the observed relative enrichments.

Finally, C_2N_2 has the shortest photochemical lifetime of the major nitrile species so should be the most enriched in the north. However, C_2N_2 appears to be less enriched than longer-lifetime HC_3N . This could be caused by having loss processes somewhat offset by an additional source term due to galactic cosmic rays in the stratosphere.

Acknowledgments

This research was funded by the UK Science and Technology Facilities Council and the NASA Cassini program. The authors thank the CIRS instrument team for their ongoing efforts, which this research relies upon. We are also very grateful to two anonymous reviewers whose comments helped to improve the manuscript.

References

- Achterberg, R.K., Conrath, B.J., Gierasch, P.J., Flasar, F.M., Nixon, C.A., 2008. Titan's middle-atmospheric temperatures and dynamics observed by the Cassini Composite Infrared Spectrometer. *Icarus* 194, 263–277.
- Blanquet, G., Walrand, J., Dangnhu, M., 1992. Absolute line-intensities of the ν_9 band of propyne at 15.5 μm . *Spectrochim. Acta* 48, 1231–1233.
- Bode, J.H.G., Smit, W.M.A., Visser, T., Verkruisje, H.D., 1980. The absolute infrared intensities of propyne- d_0 and propyne- d_3 . *J. Chem. Phys.* 72, 6560–6570.
- Borysow, A., 1991. Modelling of collision-induced infrared-absorption spectra of H_2-H_2 pairs in the fundamental band at temperatures from 20 K to 300 K. *Icarus* 92 (2), 273–279.
- Borysow, A., Frommhold, L., 1986a. Collision-induced rototranslational absorption spectra of N_2-N_2 pairs for temperatures from 50 to 300 K. *Astrophys. J.* 311, 1043–1057.
- Borysow, A., Frommhold, L., 1986b. Theoretical collision-induced rototranslational absorption spectra for modelling Titan's atmosphere: H_2-N_2 pairs. *Astrophys. J.* 303, 495–510.
- Borysow, A., Frommhold, L., 1986c. Theoretical collision-induced rototranslational absorption spectra for the outer planets: H_2-CH_4 pairs. *Astrophys. J.* 304, 849–865.
- Borysow, A., Frommhold, L., 1987. Collision-induced rototranslational absorption spectra of CH_4-CH_4 pairs at temperatures from 50 to 300 K. *Astrophys. J.* 318, 940–943.
- Borysow, A., Tang, C., 1993. Far infrared CIA spectra of N_2-CH_4 pairs for modelling of Titan's atmosphere. *Icarus* 105, 175–183.
- Capone, L.A., Dubach, J., Prasad, S.S., Whitten, R.C., 1983. Galactic cosmic-rays and N_2 dissociation on Titan. *Icarus* 55, 73–82.
- Clarke, D.W., Ferris, J.P., 1996. Mechanism of cyanoacetylene photochemistry at 185 and 254 nm. *J. Geophys. Res.* 101 (E3), 7575–7584.
- Coustenis, A., Bézard, B., 1995. Titan's atmosphere from Voyager infrared observations. IV. spatial variations of temperature and composition. *Icarus* 115, 126–140.
- Coustenis, A., Achterberg, R.K., Conrath, B.J., Jennings, D.E., Marten, A., Gautier, D., Nixon, C.A., Flasar, F.M., Teanby, N.A., Bézard, B., Samuelson, R.E., Carlson, R.C., Lellouch, E., Bjoraker, G.L., Romani, P.N., Taylor, F.W., Irwin, P.G., Fouchet, T., Hubert, A., Orton, G.S., Kunde, V.G., Vinatier, S., Mondellini, J., Abbas, M.M., Courtin, R., 2007. The composition of Titan's stratosphere from Cassini/CIRS mid-infrared spectra. *Icarus* 189, 35–62.
- Coustenis, A., Salama, A., Schulz, B., Ott, S., Lellouch, E., Encrenaz, T., Gautier, D., Feuchtgruber, H., 2003. Titan's atmosphere from ISO mid-infrared spectroscopy. *Icarus* 161, 383–403.
- de Kok, R., Irwin, P.G.J., Teanby, N.A., Lellouch, E., Bézard, B., Vinatier, S., Nixon, C.A., Fletcher, L., Howett, C., Calcutt, S.B., Bowles, N.E., Flasar, F.M., Taylor, F.W., 2007a. Oxygen compounds in Titan's stratosphere as observed by Cassini CIRS. *Icarus* 186, 354–363.
- de Kok, R., Irwin, P.G.J., Teanby, N.A., Nixon, C.A., Jennings, D.E., Fletcher, L., Howett, C., Calcutt, S.B., Bowles, N.E., Flasar, F.M., Taylor, F.W., 2007b. Characteristics of Titan's stratospheric aerosols and condensate clouds from Cassini CIRS far-infrared spectra. *Icarus* 191, 223–235.
- Flasar, F.M., Kunde, V.G., Abbas, M.M., Achterberg, R.K., Ade, P., Barucci, A., Bézard, B., Bjoraker, G.L., Brasunas, J.C., Calcutt, S., Carlson, R., Esarsky, C.J.C., Conrath, B.J., Coradini, A., Courtin, R., Coustenis, A., Edberg, S., Edgington, S., Ferrari, C., Fouchet, T., Gautier, D., Gierasch, P.J., Grossman, K., Irwin, P., Jennings, D.E., Lellouch, E., Mamoutkine, A.A., Marten, A., Meyer, J.P., Nixon, C.A., Orton, G.S., Owen, T.C., Pearl, J.C., Prange, R., Raulin, F., Read, P.L., Romani, P.N., Samuelson, R.E., Segura, M.E., Showalter, M.R., Simon-Miller, A.A., Smith, M.D., Spencer, J.R., Spilker, L.J., Taylor, F.W., 2004. Exploring the Saturn system in the thermal infrared: The Composite Infrared Spectrometer. *Space Sci. Rev.* 115, 169–297.
- Flasar, F.M., Achterberg, R.K., Conrath, B.J., Gierasch, P.J., Kunde, V.G., Nixon, C.A., Bjoraker, G.L., Jennings, D.E., Romani, P.N., Simon-Miller, A.A., Bézard, B., Coustenis, A., Irwin, P.G.J., Teanby, N.A., Brasunas, J., Pearl, J.C., Segura, M.E., Carlson, R.C., Mamoutkine, A., Schinder, P.J., Barucci, A., Courtin, R., Fouchet, T., Gautier, D., Lellouch, E., Marten, A., Prange, R., Vinatier, S., Strobel, D.F., Calcutt, S.B., Read, P.L., Taylor, F.W., Bowles, N., Samuelson, R.E., Orton, G.S., Spilker, L.J., Owen, T.C., Spencer, J.R., Showalter, M.R., Ferrari, C., Abbas, M.M., Raulin, F., Edgington, S., Ade, P., Wishnow, E.H., 2005. Titan's atmospheric temperatures, winds, and composition. *Science* 308, 975–978.
- Grecu, J.C., Winniewisser, B.P., Winniewisser, M., 1993. Absolute rovibrational line-intensities in the ν_5 band system of cyanogen, NCCN. *J. Mol. Spectrosc.* 159, 551–571.
- Horneman, V.M., 1989. Correction: Propyne at 30 μm —A line by line simulation of the ν_{10} band. *J. Mol. Spectrosc.* 137, 432.
- Horneman, V.M., Graner, G., Fakour, H., Tarrago, G., 1989. Propyne at 30 μm —A line by line simulation of the ν_{10} band. *J. Mol. Spectrosc.* 137, 1–8.
- Irwin, P., Teanby, N., de Kok, R., Fletcher, L., Howett, C., Tsang, C., Wilson, C., Calcutt, S., Nixon, C., Parrish, P., 2008. The NEMESIS planetary atmosphere radiative transfer and retrieval tool. *J. Quant. Spectrosc. Radiat. Trans.* 109, 1136–1150.
- Jacquinet-Husson, N., Scott, N.A., Chedin, A., Garceran, K., Armante, R., Chursin, A.A., Barbe, A., Birk, M., Brown, L.R., Camy-Peyret, C., Claveau, C., Clerbaux, C., Coheur, P.F., Dana, V., Daumont, L., Debacquer-Barilly, M.R., Flaud, J.M., Goldman, A., Hamdouni, A., Hess, M., Jacquemart, D., Kopke, P., Mandin, J.Y., Massie, S., Mikhailenko, S., Nemtchinov, V., Nikitin, A., Newnham, D., Perrin, A., Perevalov, V.I., Regalia-Jarlot, L., Rublev, A., Schreier, F., Schult, I., Smith, K.M., Tashkun, S.A., Teffo, J.L., Toth, R.A., Tyuterev, V.G., Auwera, J.V., Varanasi, P., Wagner, G., 2005. The 2003 edition of the GEISA/IASI spectroscopic database. *J. Quant. Spectrosc. Radiat. Trans.* 95, 429–467.
- Jolly, A., Benilan, Y., Jacquemart, D., Fayt, A., 2009. New line list for the bending modes of C_4H_2 , submitted for publication.
- Kondo, S., Koga, Y., 1978. Infrared-absorption intensities of methyl acetylene. *J. Chem. Phys.* 69, 4022–4031.
- Kunde, V.G., Aikin, A.C., Hanel, R.A., Jennings, D.E., Maguire, W.C., Samuelson, R.E., 1981. C_4H_2 , HC_3N and C_2N_2 in Titan's atmosphere. *Nature* 292, 686–688.
- Kunde, V., Ade, P., Barney, R., Bergman, D., Bonnal, J., Borelli, R., Boyd, D., Brasunas, J., Brown, G., Calcutt, S., Carroll, F., Courtin, R., Cretolle, J., Crooke, J., Davis, M., Edberg, S., Fettig, R., Flasar, M., Glenar, D., Graham, S., Hagopian, J., Hakun, C., Hayes, P., Herath, L., Horn, L., Jennings, D., Karpati, G., Kellebenz, C., Lakew, B., Lindsay, J., Lohr, J., Lyons, J., Martineau, R., Martino, A., Matsumura, M., McCloskey, J., Melak, T., Michel, G., Morell, A., Mosier, C., Pack, L., Plants, M., Robinson, D., Rodriguez, L., Romani, P., Schaefer, W., Schmidt, S., Trujillo, C., Vellacott, T., Wagner, K., Yun, D., 1996. Cassini infrared Fourier spectroscopic investigation. *Proc. Soc. Photo-Opt. Instrum. Eng.* 2803, 162–177.
- Lacis, A.A., Oinas, V., 1991. A description of the correlated k distribution method for modelling non-gray gaseous absorption, thermal emission, and multiple-scattering in vertically inhomogeneous atmospheres. *J. Geophys. Res.* 96 (D5), 9027–9063.
- Lara, L.M., Lellouch, E., Shematovich, V., 1999. Titan's atmospheric haze: The case for HCN incorporation. *Astron. Astrophys.* 341, 312–317.
- Lavvas, P.P., Coustenis, A., Vardavas, I.M., 2008. Coupling photochemistry with haze formation in Titan's atmosphere. Part II. Results and validation with Cassini/Huygens data. *Planet. Space Sci.* 56, 67–99.
- Maguire, W.C., Hanel, R.A., Jennings, D.E., Kunde, V.G., Samuelson, R.E., 1981. C_3H_8 and C_3H_4 in Titan's atmosphere. *Nature* 292, 683–686.
- McKay, C.P., 1996. Elemental composition, solubility, and optical properties of Titan's organic haze. *Planet. Space Sci.* 44, 741–747.
- Niemann, H.B., Atreya, S.K., Bauer, S.J., Carignan, G.R., Demick, J.E., Frost, R.L., Gautier, D., Haberman, J.A., Harpold, D.N., Hunten, D.M., Israel, G., Lunine, J.I., Kasprzak, W.T., Owen, T.C., Paulkovich, M., Raulin, F., Raen, E., Way, S.H., 2005. The abundances of constituents of Titan's atmosphere from the GCMS instrument on the Huygens probe. *Nature* 438, 779–784.
- Press, W.H., Flannery, B.P., Teukolsky, S.A., Vetterling, W.T., 1992. *Numerical Recipes*, 2nd ed. Cambridge Univ. Press, Cambridge.
- Teanby, N.A., Irwin, P.G.J., 2007. Quantifying the effect of finite field-of-view size on radiative transfer calculations of Titan's limb spectra measured by Cassini-CIRS. *Astrophys. Space Sci.* 310, 293–305.
- Teanby, N.A., Irwin, P.G.J., de Kok, R., Nixon, C.A., Coustenis, A., Bézard, B., Calcutt, S.B., Bowles, N.E., Flasar, F.M., Fletcher, L., Howett, C., Taylor, F.W., 2006. Latitudinal variations of HCN, HC_3N , and C_2N_2 in Titan's stratosphere derived from Cassini CIRS data. *Icarus* 181, 243–255.
- Teanby, N.A., Irwin, P.G.J., de Kok, R., Vinatier, S., Bézard, B., Nixon, C.A., Flasar, F.M., Calcutt, S.B., Bowles, N.E., Fletcher, L., Howett, C., Taylor, F.W., 2007. Vertical profiles of HCN, HC_3N , and C_2H_2 in Titan's atmosphere derived from Cassini/CIRS data. *Icarus* 186, 364–384.

- Teanby, N.A., Irwin, P.G.J., de Kok, R., Nixon, C.A., Coustenis, A., Royer, E., Calcutt, S.B., Bowles, N.E., Fletcher, L., Howett, C., Taylor, F.W., 2008. Global and temporal variations in hydrocarbons and nitriles in Titan's stratosphere for northern winter observed by Cassini/CIRS. *Icarus* 193, 595–611.
- Teanby, N.A., Irwin, P.G.J., de Kok, R., Nixon, C.A., 2009. Dynamical implications of seasonal and spatial variations in Titan's stratospheric composition. *Philos. Trans. R. Soc. London A* 367, 697–711.
- Tomasko, M.G., Bézard, B., Doose, L., Engel, S., Karkoschka, E., Vinatier, S., 2008a. Heat balance in Titan's atmosphere. *Planet. Space Sci.* 56, 648–659.
- Tomasko, M.G., Doose, L., Engel, S., Dafoe, L.E., West, R., Lemmon, M., Karkoschka, E., See, C., 2008b. A model of Titan's aerosols based on measurements made inside the atmosphere. *Planet. Space Sci.* 56, 669–707.
- Vinatier, S., Bézard, B., Fouchet, T., Teanby, N.A., de Kok, R., Irwin, P.G.J., Conrath, B.J., Nixon, C.A., Romani, P.N., Flasar, F.M., Coustenis, A., 2007. Vertical abundance profiles of hydrocarbons in Titan's atmosphere at 15° S and 80° N retrieved from Cassini/CIRS spectra. *Icarus* 188, 120–138.
- Wilson, E.H., Atreya, S.K., 2004. Current state of modelling the photochemistry of Titan's mutually dependent atmosphere and ionosphere. *J. Geophys. Res.* 109, E06002.